# FAR-INFRARED BANDS IN PLASMONIC METAL-INSULATOR-METAL ABSORBERS OPTIMIZED FOR LONG-WAVE INFRARED

by

RACHEL NEEL EVANS
B.S. Belmont University, 2016

A thesis submitted in partial fulfillment of the requirements
for the degree of Master of Science
in the Department of Physics
in the College of Sciences
at the University of Central Florida
Orlando, Florida

Summer Term
2018

Major Professor: Robert E. Peale

© 2018 Rachel Neel Evans

## ABSTRACT

Metal–insulator–metal (MIM) resonant absorbers comprise a conducting ground plane, a thin dielectric, and thin separated metal top-surface structures. Long-wave infrared (LWIR) fundamental absorptions are experimentally shown to be optimized for a ratio of dielectric thickness to top-structure dimension $t/l > 0.08$. The fundamental resonance wavelength is predicted by different analytic standing-wave theories to be ~2n$l$, where n is the dielectric refractive index. Thus, for the dielectrics $SiO_2$, AlN, and $TiO_2$, $l$ values of a few microns give fundamentals in the 8-12 micron LWIR wavelength region. Agreement of observed fundamental resonance wavelength with theory is better for $t/l >$ ~0.2. Harmonics at shorter wavelengths are always observed, but we show that there are additional resonances in the far-infrared 20-50 micron wavelength range, well beyond the predicted fundamental. These appear to be due to dispersion. They may impact selectivity in spectral sensing applications.

# ACKNOWLEDGEMENTS

First, I would like to thank my advisor Dr. Peale for advising and guiding me in my research. Without his knowledge and patience, this project would not have been possible. He has embodied what a mentor should be, and I thank him for his support.

I would also like to thank my committee Dr. Masahiro Ishigami and Dr. Arkadiy Lykah for their acceptance and guidance of this thesis.

I want to thank my lab mate Mr. Seth Calhoun for his assistance in fabrication and analysis necessary for this thesis.

I owe a special thanks to the Air Force Research Laboratory (AFRL) as well as the UCF Physics Department for financially supporting this study.

I would like to thank Dr. Justin Cleary and Dr. Evan Smith from AFRL for their continuous help and support, specifically for their extensive efforts to fabricate the measured MIM samples.

I would like to thank my friends who chose to remain my friends even during the ups and downs of graduate school, specifically Cody Barnhart, Sarah Egendoerfer, Savana Hodge, Libby Ligon, Andrew Malfavon, and Kelsey Worsham.

I especially want to thank my roommate Hannah Mitchell who always cheered me up as I worked on this project.

I would like to thank my family for their constant love and encouragement. Above all, my parents John and Dawn Evans, my brother Joshua Evans, and my grandmothers Ann Spencer and Fern Williams, have made all this work meaningful.

# TABLE OF CONTENTS

TABLE OF CONTENTS .................... v

LIST OF FIGURES .................... vi

INTRODUCTION .................... 1

THEORY .................... 2

Gap Plasmons .................... 2

LC circuit theory .................... 4

Standing Wave Resonances .................... 5

EXPERIMENTAL DETAILS .................... 6

RESULTS .................... 7

$SiO_2$ .................... 7

$TiO_2$ .................... 13

AlN .................... 17

Optimizing Absorptance .................... 21

SUMMARY .................... 23

LIST OF REFERENCES .................... 24

## LIST OF FIGURES

Figure 1: Cross-section diagram of MIM structure ........................................................ 2

Figure 2: Gap plasmon dispersion relation of $SiO_2$ and Au.......................................................... 3

Figure 3: SEM image of sample with t = 300 nm and l = 4.0 µm ................................................ 7

Figure 4: $SiO_2$ spectra grouped by square size l and arranged in ascending order of thickness t... 8

Figure 5: $SiO_2$ spectra grouped by thickness t and arranged in ascending order of square size l... 9

Figure 6: Comparison of experiment to theory for $SiO_2$-based MIM structures vs thickness t.... 10

Figure 7: $SiO_2$-based MIM spectrum from near- to far-IR ......................................................... 11

Figure 8: Stacked Far-IR $SiO_2$ plots for all samples grouped by thickness................................. 12

Figure 9: $SiO_2$-based MIM graphical solution for fundamental .................................................. 13

Figure 10: $TiO_2$ spectra grouped by thickness t and arranged in ascending order of square size l

.......................................................................................................................................... 14

Figure 11: Comparison of experiment to theory for $TiO_2$-based MIM structures. ...................... 15

Figure 12: Mid- to far-infrared spectrum of $TiO_2$ -based MIM.................................................. 16

Figure 13: Stacked Far-IR $TiO_2$ plots for all samples grouped by thickness............................... 16

Figure 14: Graphical solution for $TiO_2$-based MIM .................................................................... 17

Figure 15: AlN-based MIM reflectance spectra ............................................................................ 18

Figure 16: Comparison of experiment to theory for AlN-based MIM structures. ...................... 18

Figure 17: AlN-MIM reflectance spectrum ..................................................................................... 19

Figure 18: Stacked Far-IR AlN plots for all samples grouped by thickness ................................ 20

Figure 19: Index spectrum of AlN with hypothesized extension ................................................. 21

Figure 20: Absorptance for $SiO_2$, $TiO_2$, and AlN in the LWIR region......................................... 22

Figure 21: Far-IR absorptance for $SiO_2$- and AlN-based MIMs vs. t/l........................................ 22

# INTRODUCTION

Metal–insulator–metal (MIM) resonant infrared absorbers are thin film structures that can be fabricated by contact photolithography for night vision (8–12 µm wavelength long-wave infrared, LWIR) and target tracking (3-5 µm wavelength mid-wave infrared, MWIR) applications. They have been applied to IR bolometers[1] and to pyroelectric detectors.[2]

Our group recently published[3] a comprehensive study of MIM absorbers at 50 µm wavelength in the far-IR spectral region, where the dispersion of the insulator ($SiO_2$) was weak. The resulting resonant absorption spectrum was simple and accurately agreed with the analytic standing-wave model introduced in that paper. This thesis investigates MIM absorbers for LWIR, where dispersion can be strong. Our group recently published a study of the effect of such dispersion by considering MIMs fabricated with three different dielectrics, namely $SiO_2$, $TiO_2$, and AlN.

The main theme of this thesis is to investigate the range of geometrical MIM parameters that optimize the fundamental absorption strength. A second objective is to determine the limits for these parameter values for the applicability of our preferred analytic theory. A third objective is to reveal how dispersion at wavelengths beyond the range of interest can give rise to unwanted resonances there.

## THEORY

Gap Plasmons

Figure 1 depicts a two-dimensional (2D) schematic cross-section of the MIM structures fabricated. These devices comprise a metal ground plane, dielectric, and patterned metal squares as the top layer. The dielectric thickness *t* and top-square dimension *l* are indicated. The metals are optically thick, usually ~200 nm. Infrared radiation is incident from above. At certain wavelengths it excites resonances with strong fields in the dielectric under each of the squares, which can lead to nearly total absorption of the incident light.

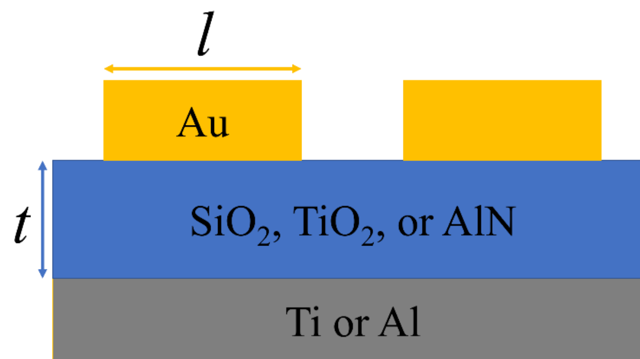


Figure 1: Cross-section diagram of MIM structure

This section describes three different analytic theories that have been invoked to explain the resonances and to calculate their wavelengths. The different theories have different dependences on the geometrical parameters and optical constants. The first we consider is a model based on standing waves of so-called gap plasmons. Gap plasmons appear first to have been considered in calculating the van der Waals attraction between two metal plates[4,5]. The resonance condition would be defined by standing gap plasmon waves with wavevector determined by the dimension of the spatially-finite top metal. Knowing the dispersion relation ω

vs $k_p$, we can find the resonance frequencies for the $k_p$ values that correspond to the standing waves. The dispersion relation was calculated[4] by considering two conducting media separated by a dielectric thickness of $t$ and wavevector for x-propagation $k_p$. The nonretarded solutions of the Laplace equation yield Eq. (1)

$$\left(\frac{1+\varepsilon(\omega)}{1-\varepsilon(\omega)}\right)^2 e^{2k_p t} - 1 = 0 \tag{1}$$

where $\varepsilon(\omega)$ is the ratio of conductor and dielectric permittivities, $\varepsilon_m(\omega)/\varepsilon_d(\omega)$. We consider that the permittivity of the metal $\varepsilon_m(\omega)$ is complex but the permittivity of the dielectric $\varepsilon_d(\omega)$ is real. The wave vector $k_p$ for x propagation is complex, but the real part should give the standing-wave resonance condition. This is given by

$$k_p{}' = \frac{1}{4t} ln\left[\frac{1+|\varepsilon(\omega)|^2 + 2|\varepsilon'(\omega)|^2}{1+|\varepsilon(\omega)|^2 - 2|\varepsilon'(\omega)|^2}\right] \tag{2}$$

Figure 2 presents a plot of $\omega$ vs $k_p$ from Eq. (2), supposing $SiO_2$ and Au as our media with empirical values of $\varepsilon(\omega)$ from published permittivity spectra[6]. Thickness $t$ is assumed to have the value 0.5 µm, which is typical of our experiments.

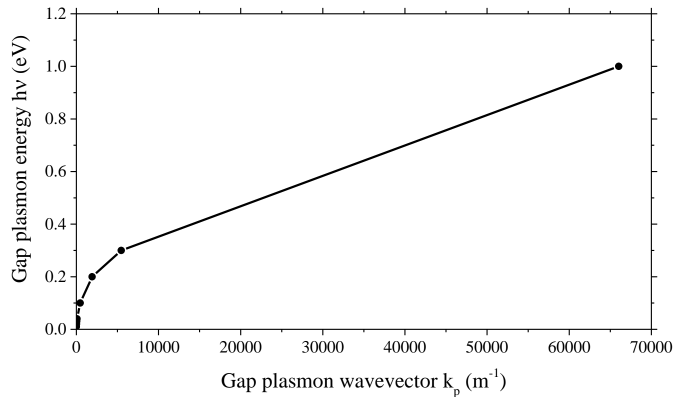


Figure 2: Gap plasmon dispersion relation of $SiO_2$ and Au.

The fundamental wavevector should satisfy boundary conditions that have nodes at the edges or a node at the center of the conducting square. Either condition gives a wavevector for the fundamental resonance of $4\pi/l$. Supposing $l$ has a typical value 4 μm, we get the smallest allowed wavevector $k_p = \pi \times 10^6$ m$^{-1}$, which is well beyond the range of Figure 2. Thus, the fundamental resonance is predicted by this theory to be above 1 eV, and that is nearly in the visible spectral range.

LC circuit theory

Another published theory[7] models the cavity as an LC circuit. Then[3] the resonant frequency is

$$f = \frac{\sqrt{2}}{2\pi\sqrt{LC}} \tag{3}$$

The inductance $L$ is estimated by assuming the square and ground plane are connected at the square's edges via displacement current to form a rectangular solenoid. $C$ is a capacitance formed by half of the square with the ground plane. Both $L$ and $C$ depend on the thickness of dielectric $t$, size of absorber $l$, permeability, and dielectric permittivity according to $L = \mu_0\mu_r t$ and $C = \varepsilon_0\varepsilon_r l^2/2t$. At infrared frequencies $\mu_r = 1$. From the expressions for $L$ and $C$ and Eq. (3), the fundamental resonance wavelength is

$$\lambda = \pi\, l\, \mathrm{n}(\lambda) \tag{4}$$

This theory does not predict the appearance of harmonics, does not depend on dielectric thickness, and it treats the metals as perfect conductors. The resonance wavelength is found graphically from a plot of n(λ) vs λ by finding the intersection of that curve with a line having

slope $1/\pi l$ and zero intercept. The predicted resonances are close to the fundamentals observed, but the agreement is worse than provided by the next theory.

## Standing Wave Resonances

Our group proposed[8] a theory based on standing plane waves in the MIM waveguide with odd number of transverse reflections. It has been shown to work perfectly in the far-IR, including the prediction of harmonics, for $t/l$ ratios in the range 0.09 to 0.46. Multiple resonances are found from graphical solution of

$$\lambda(b, m) = \frac{2n(\lambda)}{b + 2m}\sqrt{l^2 + (b+1)^2 t^2} \tag{5}$$

where m is an integer and b is the odd integer number of reflections. For the fundamental $(b,m) = (1,0)$, if $t \ll l$, this gives a value similar to the LC circuit model except that $\pi$ is replaced by 2. This theory does depend on dielectric thickness, but it also considers the metals to be perfect conductors. In contrast to the gap plasmon picture, this theory is based on rays with a transverse momentum component. The ray picture is assumed even though the wavelengths considered are far beyond cut-off for TM modes in the parallel-plate waveguide formed by square and ground plane. This thesis is primarily concerned with the fundamental resonance given by

$$\lambda(1,0) = 2n\sqrt{l^2 + 4t^2} \tag{6}$$

# EXPERIMENTAL DETAILS

Ti, Au, $SiO_2$ and $TiO_2$ layers were deposited on glass or silicon substrates using electron beam evaporation. Al and AlN were deposited using an aluminum target in a DC magnetron sputtering system (MRC). AlN was reactively sputtered in nitrogen partial pressure. Standard photolithography and lift-off techniques were used to pattern the top metals. On all samples, a thin layer of Ti was deposited before the top Au film as a sticking layer. $SiO_2$ samples were created with $t$ values of 100, 200, 300, 500, and 1000 nm. $TiO_2$ samples had $t$ values of 100, 200, and 300 nm. AlN samples had a thickness of either 212 or 246 nm. For samples fabricated using e-beam evaporation, thicknesses were measured via crystal monitor, while sputtered film thicknesses were based on calibrated deposition rates. Thicknesses of all dielectric films were confirmed using Filmetrix optical profilometer.

Reflectivity spectra were collected using a BOMEM DA8 Fourier-transform spectrometer at near normal incidence. Spectrometer resources for the far-IR (20-50 μm wavelengths) included a Globar source, 3 micron mylar pellicle beamsplitter, and DTGS pyroelectric detector. For shorter wavelengths (2-20 μm) the beamsplitter was changed to KBr and the detector to a 77 K HgCdTe photoconductor (MCT).

# RESULTS

## $SiO_2$

Figure 3 presents a scanning electron microscope image of gold squares patterned on an $SiO_2$ sample. Such images were used to determine the square dimension *l* for every sample. The observed rounding of the corners is a common fabrication artifact. The smaller fabricated squares can become almost circular. The effect of this rounding remains unclear, but it may account for the increasing deviation from theory as fundamental resonance wavelength is decreased.

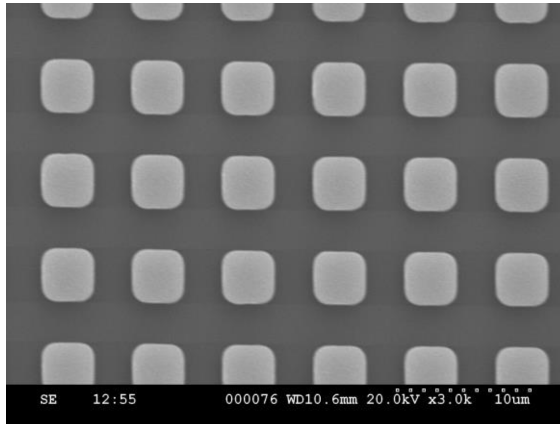


Figure 3: SEM image of sample with $t$ = 300 nm and $l$ = 4.0 µm

Figure 4 and Figure 5 present stacked spectra for $SiO_2$–based MIM devices. Figure 4 groups the data according to square size *l*, and guide lines indicate the longest wavelength bands as they shift with changing *t*. The observed complexity of these spectra is expected due to high LWIR dispersion for $SiO_2$.[9] There are multiple solutions for the same $(b,m)$ = (1,0) values, and it is difficult to unambiguously identify the different bands. The red guide lines indicate the longest LWIR fundamental resonance wavelength, which will be considered in Figure 6 and

Figure 7. For $l$ = 2.5 μm, the identification of the longest wave fundamental is ambiguous, because it appears to pass through another band, which was observed in all samples, and which remained fixed as $t$ changes. The guideline shown for those samples follows a band that gives similar behavior as for samples with $l$ = 4.0 and 4.5 μm.

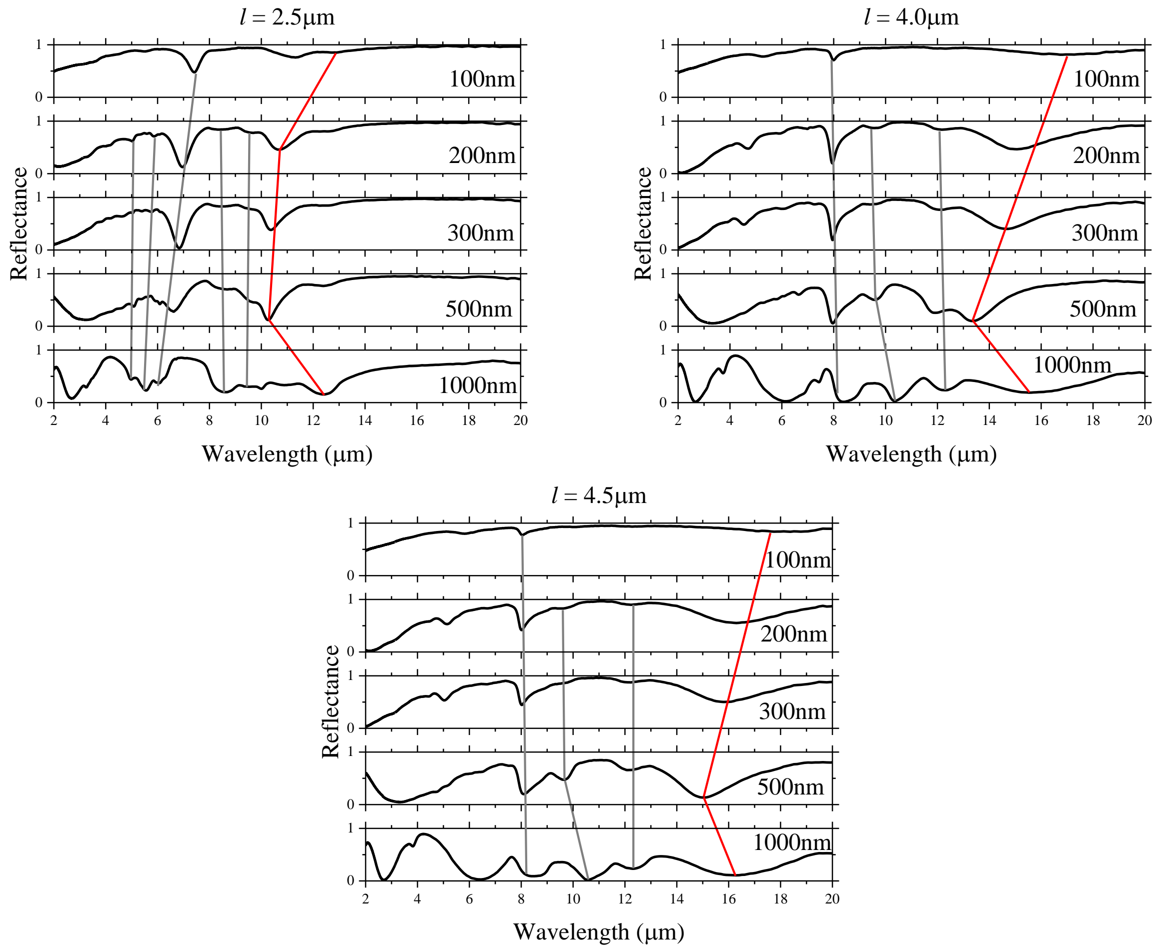


Figure 4: $SiO_2$ spectra grouped by square size $l$ and arranged in ascending order of thickness $t$

Figure 5 presents the data grouped together by thickness $t$ to better demonstrate the $l$ dependence. The fundamental shifts to shorter wavelength as $l$ is decreased. For the smallest $l$ value, the identity of the fundamental becomes somewhat ambiguous. All three plots have a band just above 12 microns, and the fundamental appears to pass through that unmoving band as $l$ is decreased from 4.0 to 2.5 µm.

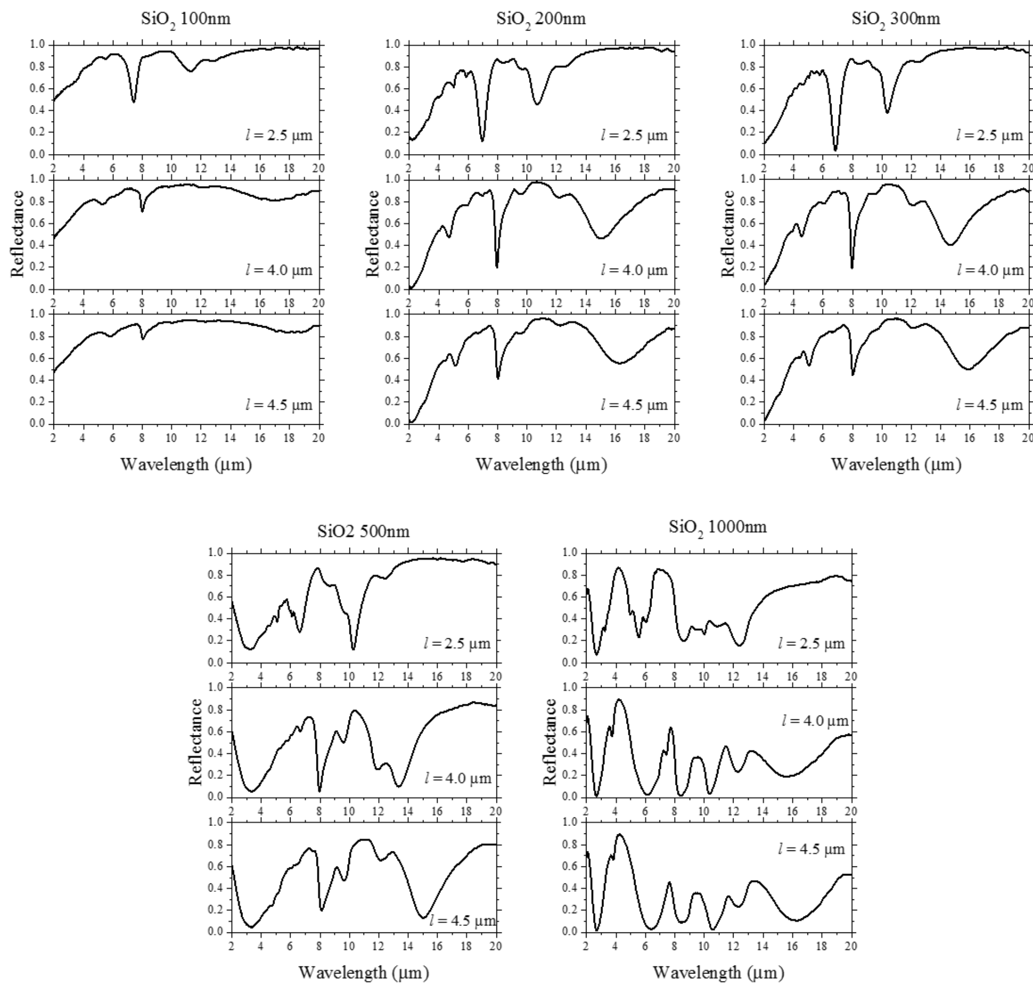


Figure 5: $SiO_2$ spectra grouped by thickness $t$ and arranged in ascending order of square size $l$

Figure 6 presents a summary of observed absorption resonances for fabricated $SiO_2$ MIM devices plotted as a function of *t*. The longest wave line that exhibits strong absorption is considered to be the fundamental in Figure 6. This selection is partly based on agreement with theory and comparison to the other curves in the ambiguous *l* = 2.5 µm case.

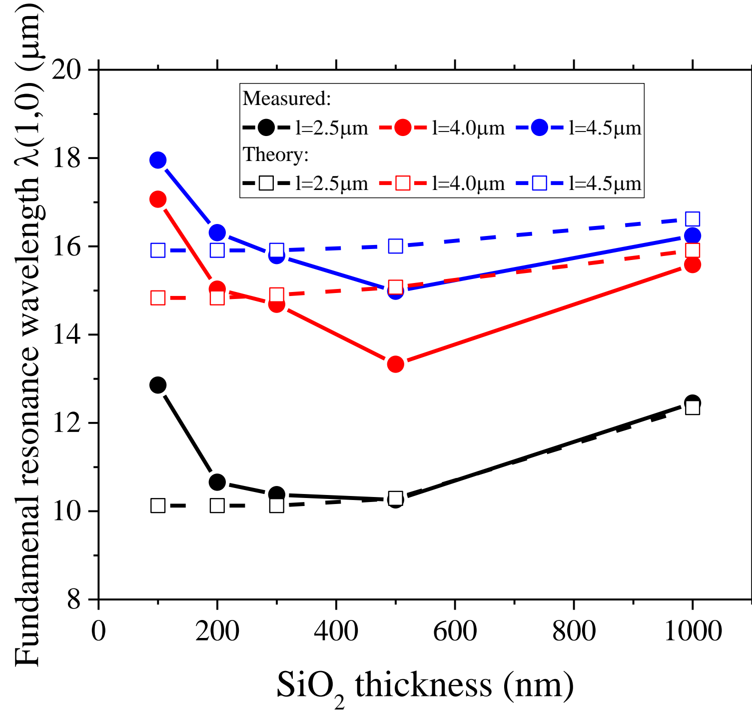


Figure 6: Comparison of experiment to theory for $SiO_2$-based MIM structures vs thickness *t*

For *l* = 2.5 µm, the agreement between experiment and theory is good for *t/l* ratios > 0.2. For *l* = 4.0 and 4.5 µm, the *t/l* ratio never reaches that value, but it is clear that the experimental values begin to approach the theoretical ones at the largest *t/l*. Previously studied devices[9] were fabricated with poor control over *l* values, so the results were focused on a relationship between the fundamental resonance wavelength and the geometrical factor presented in Eq. (6). That

study showed that agreement became worse when $\sqrt{l^2 + 4t^2}$ became smaller. This might be due to the increased circularization of the squares at the smaller dimensions. Since this geometric factor includes both *l* and *t* dependence, the precise dependence on *t* was previously unattainable due to poor *l* control. The range of *t*-values was anyway much more limited than here.

Figure 7 shows the full spectrum for both the LWIR (red line) and far-IR (black line) for one $SiO_2$ MIM sample. Figure 7 reveals a new strong band at 24 microns in the Far-IR region. This is outside the intended LWIR operation region, and hence may degrade wavelength selectivity for spectral sensing applications.

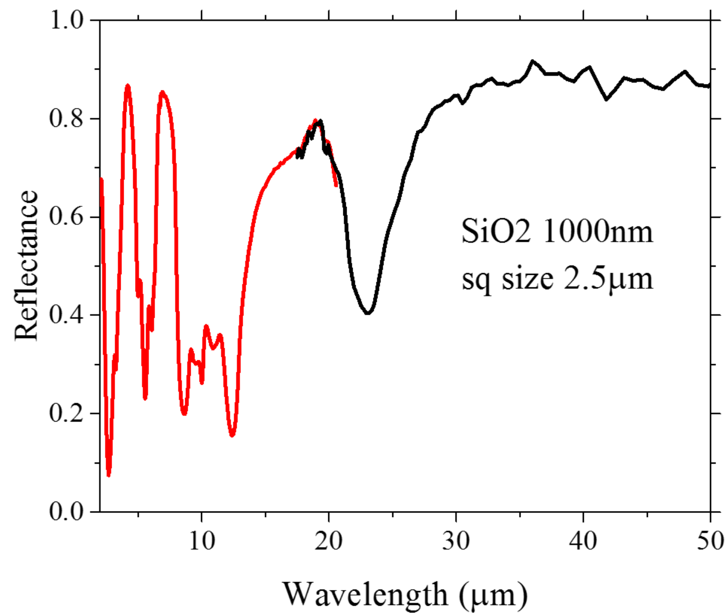


Figure 7: $SiO_2$-based MIM spectrum from near- to far-IR

Figure 8 presents far-IR reflectance spectra for all of the $SiO_2$ samples. The observed band strengthens with increasing *t/l*, as did the LWIR bands. The resonance wavelength also red

shifts with increasing *l* for given *t*, but only weakly, suggesting that it may be anchored to a dispersion feature.

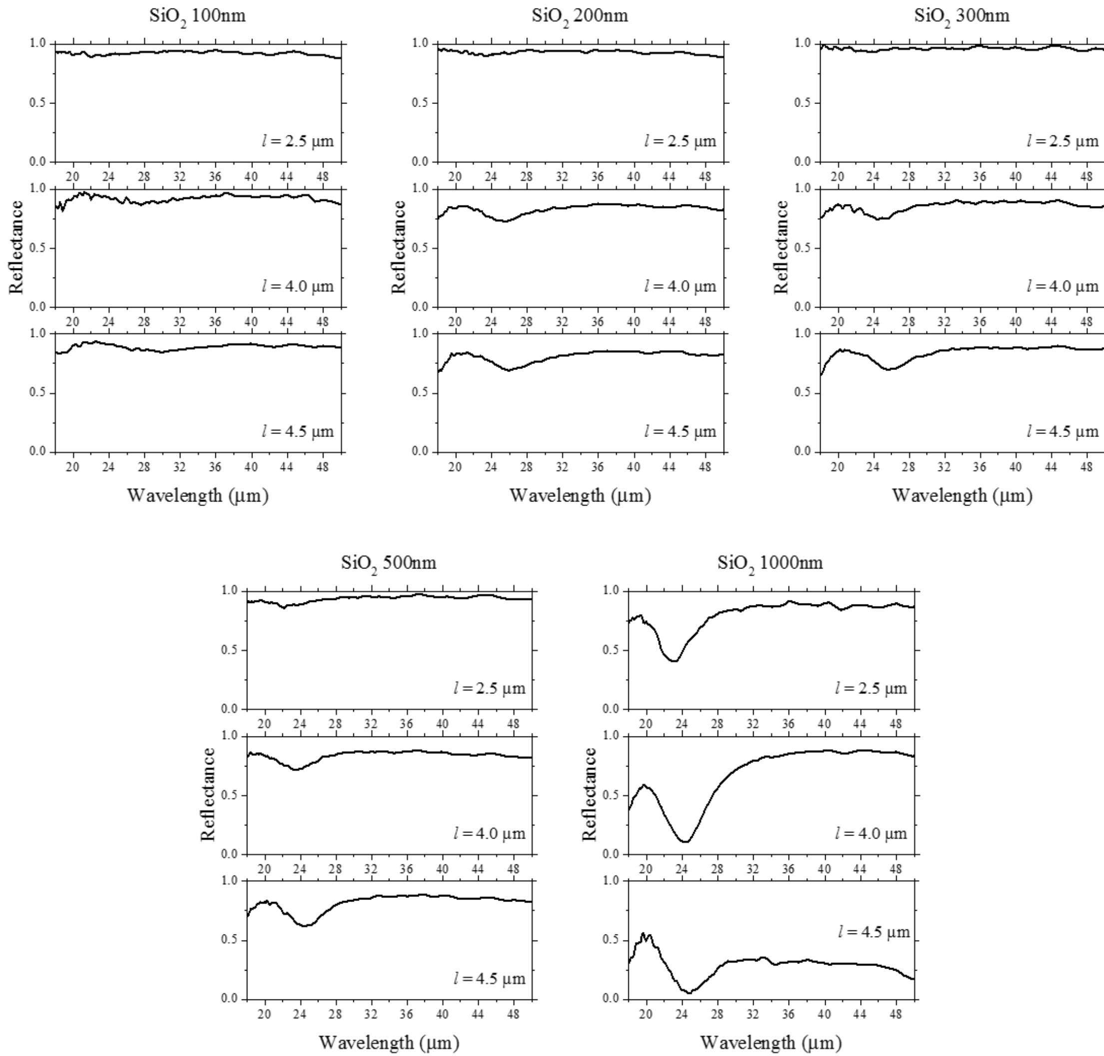


Figure 8: Stacked Far-IR $SiO_2$ plots for all samples grouped by thickness

Figure 9 presents the index spectrum for $SiO_2$ plotted[10] with the theoretical curve for graphical solution of Eq. (6) using *l,t* values indicated in Figure 7. The multiple intersections in the LWIR are due to dispersion and explain the complexity of the absorption spectrum there.

There is an additional far-IR dispersion feature in the published index spectrum that the theory line nearly intersects near 24 microns, right where the far-IR absorption band occurs. In is clear from the kinks in the index spectrum that it is of low spectral resolution, so that the peak of the dispersion feature may well be higher. Thus, uncertainty in the slope of the line and in the index spectrum suggest that an intersection is certainly possible, which would explain the observed 24 μm band.

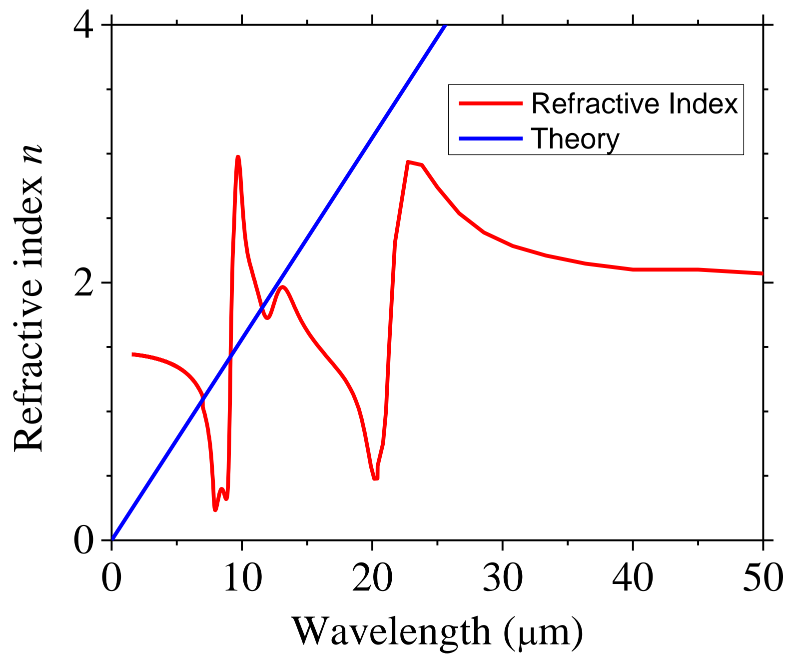


Figure 9: $SiO_2$-based MIM graphical solution for fundamental

<u>$TiO_2$</u>

Figure 10 is a collection of all LWIR spectra taken for $TiO_2$. Only three $TiO_2$ thicknesses (100, 200, and 300 nm) were used in the fabricated MIM devices that were subsequently measured. Precise control over *l* was more difficult for the $TiO_2$ MIM samples because these were fabricated on a glass slide substrate rather than silicion wafer. Duirng the photolithography

process when photoresist (PR) is spun onto the sample, the rectangular glass slides form a less uniform thickness of PR across the substrate compared to circular silicon wafers, resulting in less repeatable *l* values. Because there can be non-uniformity in *l* value across the sample, the IR beam may probe a portion of the sample where the *l* values differ from those determined at a given spot by SEM imaging, which leads to higher scatter and uncertainty in comparison to the results for $SiO_2$-based MIMs. A strong LWIR fundamental is not clearly observed until a thickness of at least 200 nm.

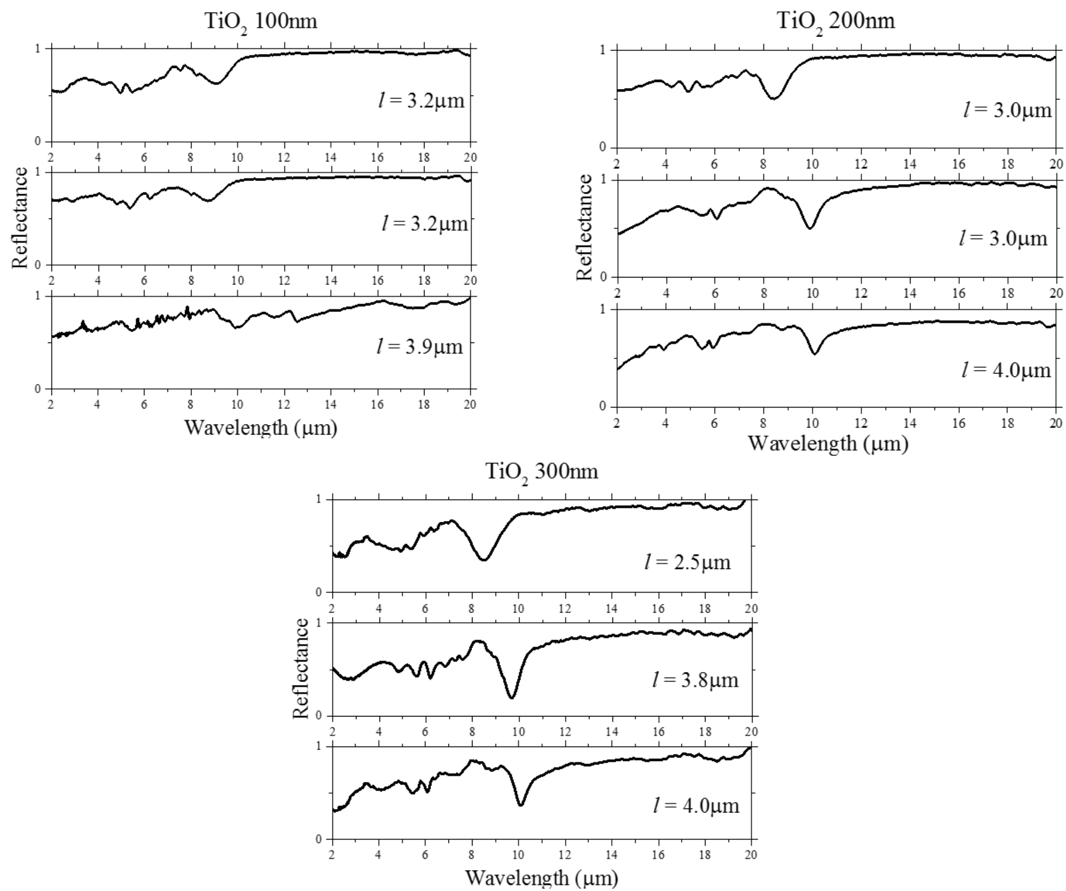


Figure 10: $TiO_2$ spectra grouped by thickness *t* and arranged in ascending order of square size *l*

Figure 11 shows the fundamental wavelengths from each $TiO_2$ sample compared to theoretical values. The experimental points (symbols) agree with the theory (lines) within the uncertainty defined by the scatter in their values.

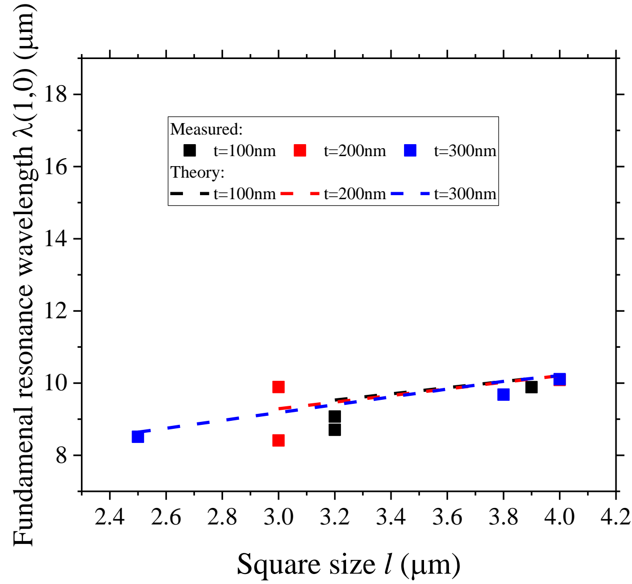


Figure 11: Comparison of experiment to theory for $TiO_2$-based MIM structures.

Figure 12 presents the full spectrum out to 50 μm wavelength for one of the $TiO_2$ samples. None of these samples show evidence of a strong absorption band beyond 50 μm, in contrast to $SiO_2$- and AlN- (see below) based MIM devices. There may be a very weak band at 20 microns and possibly the edge of a band at 50 microns.

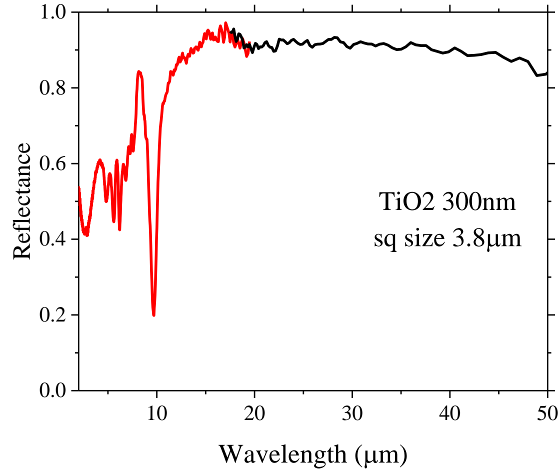


Figure 12: Mid- to far-infrared spectrum of $TiO_2$ -based MIM

Figure 13 presents all Far-IR data for $TiO_2$ samples. No strong resonances were observed for all three thickness and square size variations.

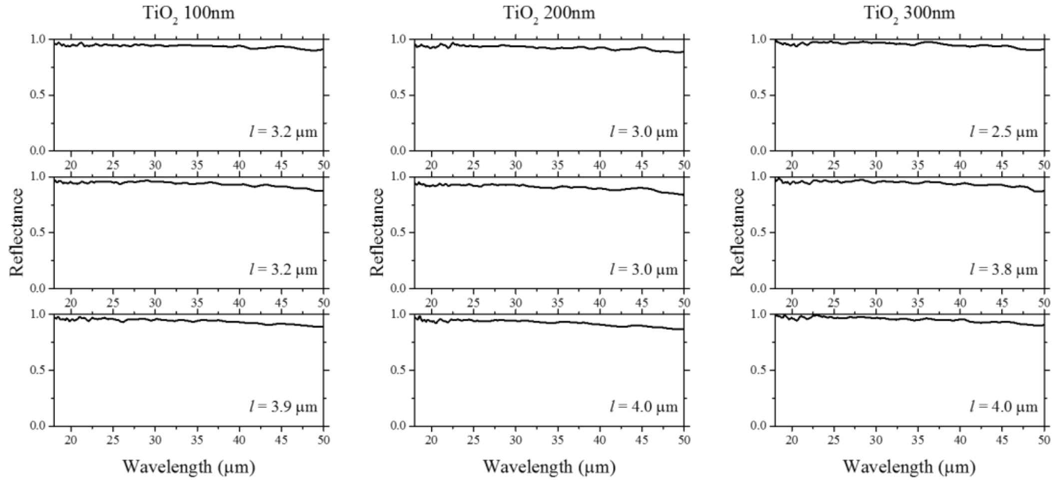


Figure 13: Stacked Far-IR $TiO_2$ plots for all samples grouped by thickness

Figure 14 presents the index spectrum of $TiO_2$ from MWIR to far-infrared.[11] The straight line is determined from Eq. (6) for the given geometrical parameters. This line shows three intersections. The first is responsible for the resonance line observed near 10 µm

wavelength. A small change of slope or difference in the index spectrum might make the other two intersections disappear, which would explain the absence of significant absorption bands beyond 20 microns. On the other hand, there may be very weak indications of bands at 20 and 50 microns, which would be near to the predicted values determined by the second pair of intersections, according to Figure 14.

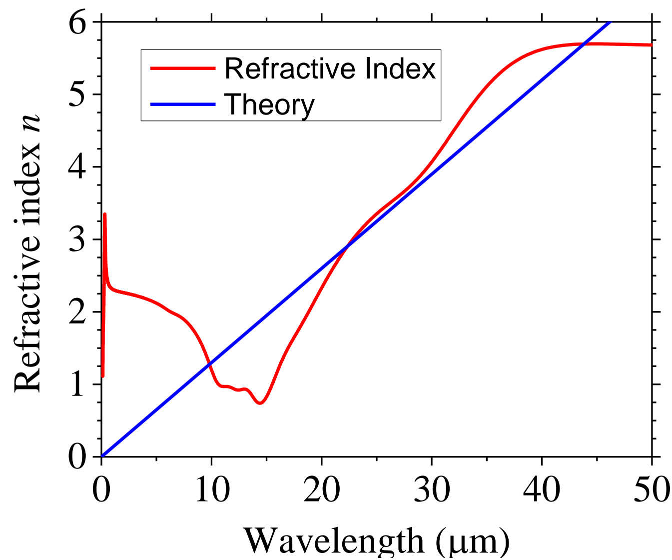


Figure 14: Graphical solution for $TiO_2$-based MIM

AlN

Figure 15 presents LWIR reflectance spectra for AlN-based MIMs. These spectra are simple with only a single strong fundamental near 10 microns due to the low LWIR dispersion of AlN compared to $SiO_2$.[9] As in the case of TiO2, the *l* values were poorly controlled during fabrication, so that the spots probed by the IR beam may have somewhat different square sizes

than those determined from SEM imaging on a single spot. This can account for the non-monotonic dependence of resonance position on *l* value.

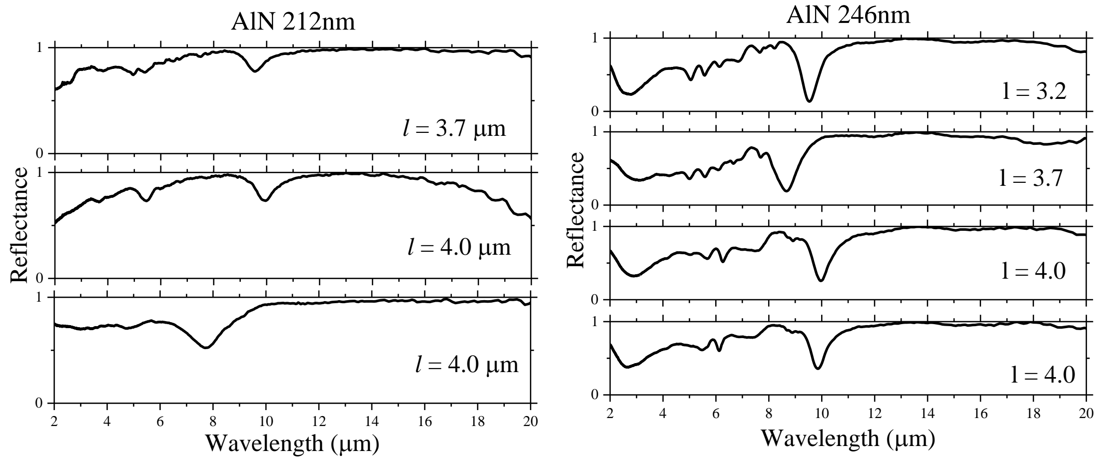


Figure 15: AlN-based MIM reflectance spectra

Figure 16 presents a summary of observed absorption resonances for fabricated AlN-MIM devices. The experimental observations agree with the theory prediction from Eq. (6) within the experimental uncertainty defined the by the scatter in the data.

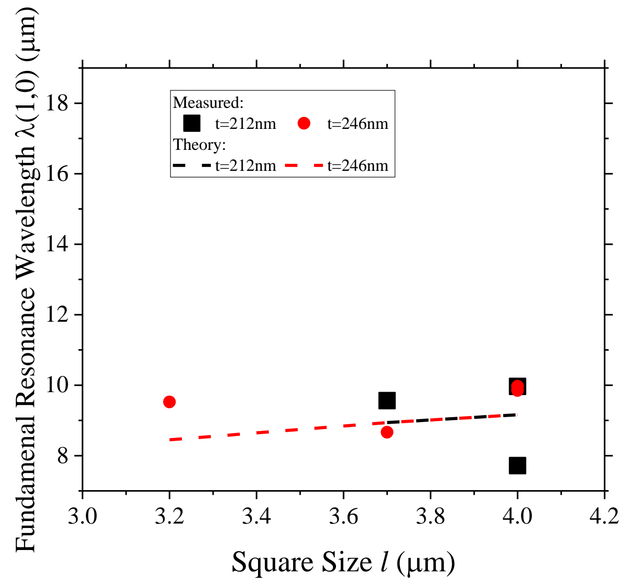


Figure 16: Comparison of experiment to theory for AlN-based MIM structures.

Figure 17 presents the near- to far-IR spectrum for one of the AlN-based MIM devices. A strong band is observed at 22 microns wavelength, similar to what was observed for the $SiO_2$-based MIMs.

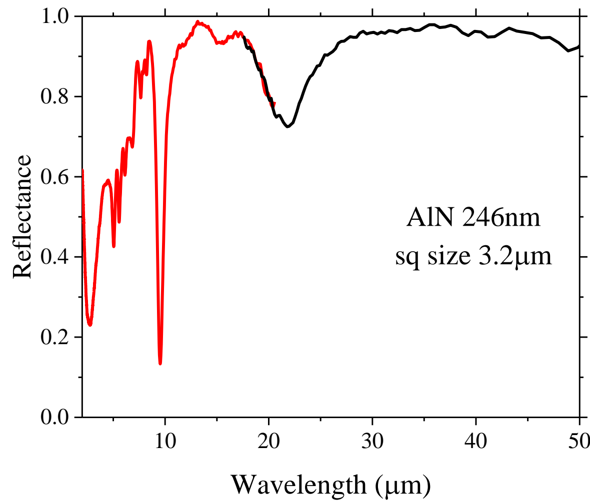


Figure 17: AlN-MIM reflectance spectrum

Figure 18 presents far-IR spectra for all AlN samples. Far-IR resonances are weak or absent for the $t$ = 212 nm samples. Far-IR resonances are stronger for the $t$ = 246 nm samples, but they do not follow a clear trend with increasing $l$, probably due to the uncertainty in their values as already mentioned. In one of the samples, the resonance appears curiously to be split.

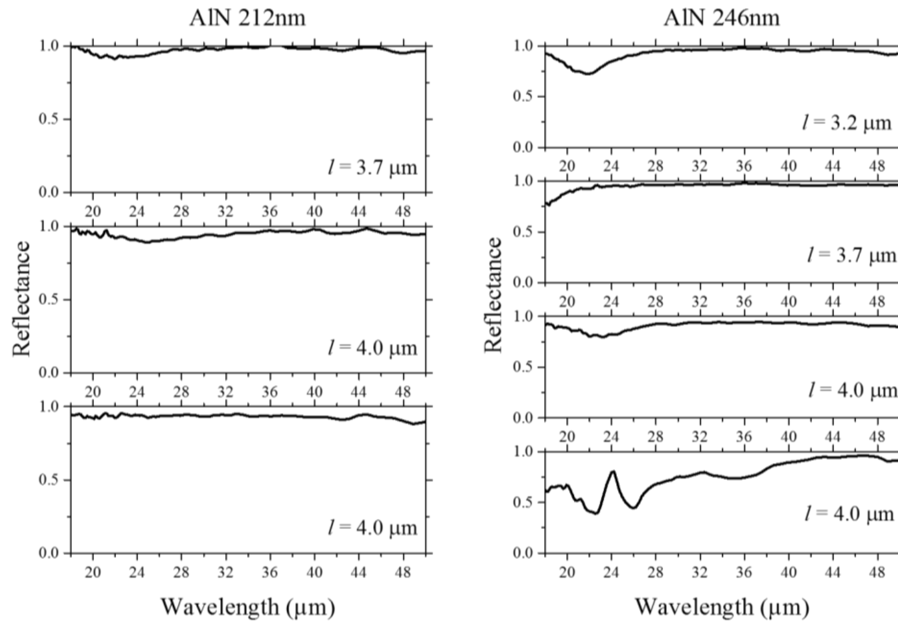


Figure 18: Stacked Far-IR AlN plots for all samples grouped by thickness

Figure 19 presents the available index spectrum for AlN, which does not extend into the far-IR. However, the far-IR extinction spectrum is available[12], and that curve is plotted, in the form of a large and sharp absorption peak. This should give rise to a strong dispersion feature in the far-IR. A sketch of a possible index spectrum in that range has been added to show how a solution at 22 microns could appear. The straight line, whose slope is the inverse of the geometrical factor in Eq. (6), would intersect that index curve, giving rise to a resonance solution close to the wavelength of the band observed in Figure 17. The short wavelength solution below 10 microns agrees with the strong sharp line in Figure 15. There is a weak dip near 15 microns In Figure 15 that may correspond to the intersection in Figure 19 with the rising portion of the index curve. There is anecdotal evidence that when the theory curve intersects a derivative like dispersion feature in the index spectrum, strong absorptions occur mainly for intersections with the downward sloping parts of the index curve and not for the intersection with the sharply rising part of the curve at the center of the feature.

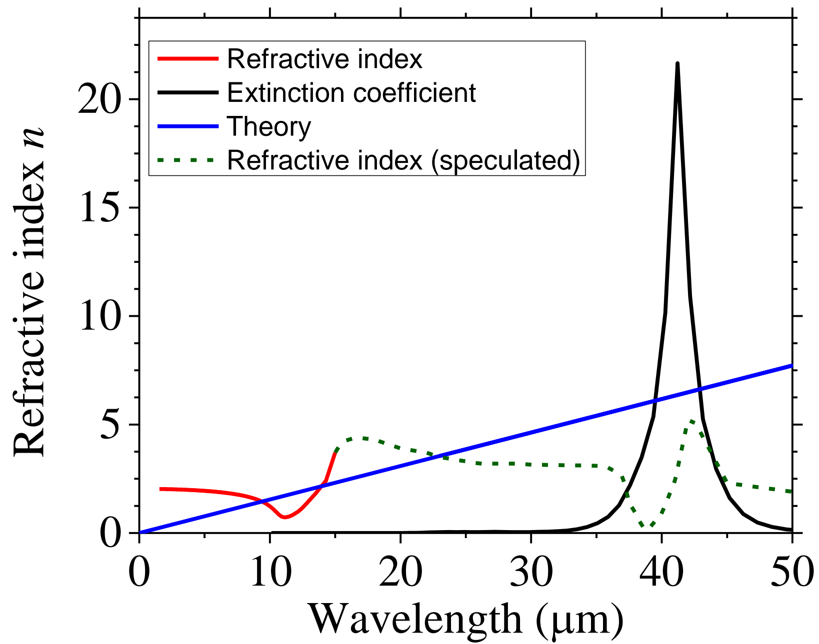


Figure 19: Index spectrum of AlN with hypothesized extension

## Optimizing Absorptance

Figure 20 presents a plot of the peak absorptance for the LWIR fundamental as a function of the ratio of *t/l* for all samples investigated in this thesis. The behavior appears to be universal, nearly independent of the dielectric used. Absorptance increases rapidly with *t/l* until about 0.08, beyond which it very slowly declines. The latter dependence is currently only available for $SiO_2$-based MIMs. $TiO_2$-based MIMs may peak at slightly higher values of *t/l*. This may be because the extinction coefficient of $TiO_2$ is much smaller in the LWIR than for either $SiO_2$ or AlN, which are similar. The index for $TiO_2$ in the LWIR is also larger than for the other two.

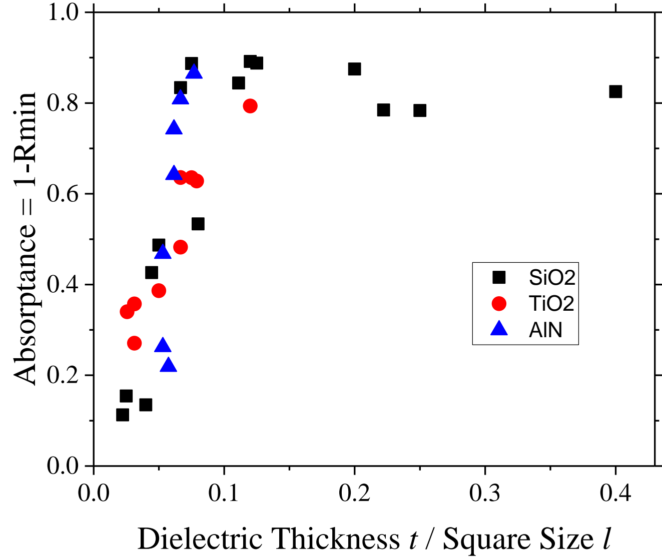


Figure 20: Absorptance for $SiO_2$, $TiO_2$, and AlN in the LWIR region

Figure 21 presents a plot of absorptance maximum for the observed far-IR bands beyond 20 micron wavelength. The strength of device absorption is plotted as a function of the *t/l* ratio. There is a tendency for absorptance to increase with *t/l*, but the dependence is less clear than for the LWIR band.

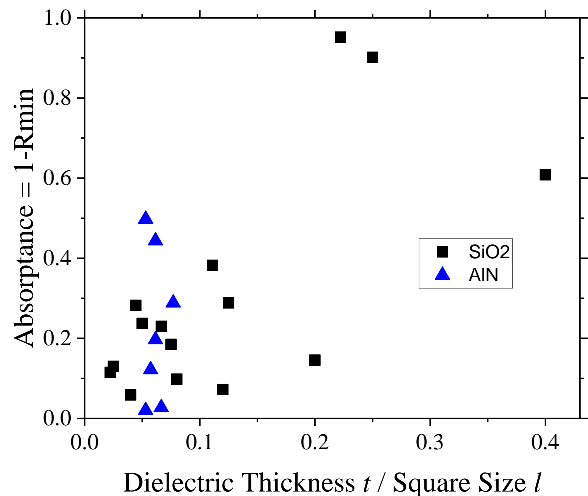


Figure 21: Far-IR absorptance for $SiO_2$- and AlN-based MIMs vs. *t/l*

## SUMMARY

Infrared reflectance spectra were collected for MIM plasmonic resonant absorbers based in $SiO_2$, AlN, and $TiO_2$ dielectrics. The fundamental resonance wavelength is reasonably well predicted by an analytic standing-wave theory introduced by our group. Agreement of observed resonance wavelength with theory is better for larger $t/l >$ ~0.2. Long-wave infrared (LWIR) fundamental absorption strength is experimentally shown to be optimized for a ratio of dielectric thickness to top-structure dimension, $t/l$, of ~0.2. In addition to the usual harmonics at shorter wavelengths, we discovered additional far-IR resonances at wavelengths well beyond the predicted LWIR fundamental, and these appear to be explained by our same model when dispersion features are accounted for.

# LIST OF REFERENCES

1. E. M. Smith, J. Nath, J. Ginn, R. E. Peale, and D. Shelton: Responsivity improvements for a vanadium oxide microbolometer using subwavelength resonant absorbers. *Proc. SPIE* **9819** (2016).
2. V. J. Gokhale, P. D. Myers, and M. Rais-Zadeh: Subwavelength plasmonic absorbers for spectrally selective resonant infrared detectors. *Proc. IEEE Sensors Conf.* Valencia, Spain (2014).
3. J. Nath, S. Modak, I. Rezadad, D. Panjwani, F. Rezaie, J.W. Cleary, and R. E. Peale: Far-infrared absorber based on standing-wave resonances in metal-dielectric-metal cavity. *Opt. Express* **23**, 20366-20380 (2015).
4. N. G. Van Kampen, B. R. A. Nijober, and K. Schram: On the macroscopic theory of Van Der Waals Forces. *Phys. Lett.* **26A**, 307-308 (1968).
5. C. Kittel: Solid State Physics, 7th edition, 319-320.
6. M. A. Ordal, R. J. Bell, R. W. Alexander, L. L. Long, M. R. Querry: Optical properties of Au, Ni, and Pb at submillimeter wavelengths. *Appl. Opt.* **26**, 744-752 (1987).
7. Y. Ye and Y. Jin, "Omnidirectional, polarization-insensitive and broadband thin absorber in the terahertz regime," JOSA B **27**, 498 (2010).
8. J. Nath, D. Maukonen, E. Smith, P. Figueiredo, G. Zummo, D. Panjwani, R. E. Peale, G. Boreman, J. W. Cleary, K. Eyink: Thin-film, wide-angle, design-tunable, selective absorber from near UV to far infrared. *Proc. SPIE* **8704**, 87041D (2013).
9. S. R. Calhoun, V. C. Lowry, R. Stack, R. N. Evans, J. R. Brescia, C. J. Fredricksen, J. Nath, and R. E. Peale: Effect of dispersion on metal-insulator-metal infrared absorption resonances. *MRS. Comm.*, 1-5 (2018).

10. J. Kischkat, S. Peters, B. Gruska, M. Semtsiv, M. Chashnikova, M. Klinkmüller, O. Fedosenko, S. Machulik, A. Aleksandrova, G. Monastyrskyi, Y. Flores, and W. T. Masselink: Mid-infrared optical properties of thin films of aluminum oxide, titanium dioxide, silicon dioxide, aluminum nitride, and silicon nitride. *Appl. Opt.* **51**, 6789-6798 (2012).

11. T. Siefke, S. Kroker, K. Pfeiffer, O. Puffky, K. Dietrich, D. Franta, I. Ohlídal, A. Szeghalmi, E.-B. Kley, A. Tünnermann: Materials pushing the application limits of wire grid polarizers further into the deep ultraviolet spectral range, *Adv. Opt. Mater*. **4**, 10.1002 (2016).

12. E. D. Palik: Handbook of Optical Constants of Solids, Academic Press, 394-396 (1997).